Paper ???

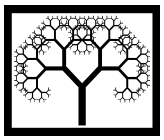

Proceedings of the First International Conference on
Railway Technology: Research, Development and Maintenance,
J. Pombo, (Editor),
Civil-Comp Press, Stirlingshire, Scotland

The Suitability of Using Accumulated Plastic Strain to Assess the Damage at the Rail-Wheel Interfaces

I.U. Wickramasinghe[1,2], D. Hargreaves[1] and D. De Pellegrin[1]
[1] School of Chemistry, Physics and Mechanical Engineering
Faculty of Science and Technology
Queensland University of Technology, Brisbane, Australia
[2] Corporate Research Centres (CRC) for Rail Innovation, Australia

Abstract

Numerous Abaqus [1] finite element analyses have been carried out using various plasticity models to investigate the effect of friction force on the rail head in relation to both the development of the accumulated plastic strain (PEEQ) and the changes in the depth of PEEQ distribution in the wheel-rail contact. The normal force distribution on the rail head was assumed to be Hertzian. The tangential force was implemented as a fraction of the normal force in the subroutine. Each analysis was carried out for a single pass and the effect of various friction coefficient values has been observed.

Keywords: plastic equivalent strain, finite element modelling, wheel-rail contact, pressure load, material plasticity, Abaqus simulations, Hertzian contact theory.

1 Introduction

The elastic behaviour of the wheel-rail contact is described using Hertzian contact theory [2]. The chapter Contact and Creep-Force Models in the book Railroad Vehicle Dynamics [3] explains the procedure of calculating Hertzian parameters by assuming an elastic model for the wheel-rail contact.
Wear and rolling contact fatigue are the sources of damage that account for most rail maintenance costs. The increasing demand for rail transport requires rail stresses to be increased to a maximum with the highest possible speed also. The wheel-rail contact occurs in an area less than $50mm^2$ and two main forces are active on the rail head: the vertical force and the friction force.
When considering two bodies in contact under a static load and with no slip *i.e.* no relative movement at the contact, there shear will not occur at the interface. Therefore the shear stress acting is equal to zero [4]. However, if the contact load is sufficiently high, then the maximum shear stress will exceed the yield stress of the material and plastic deformation place. Material will then deform along the line of

action of maximum shear stress. Principle stresses (σ_x & σ_y) & shear stress (τ) varies with the depth below the interface.
Rolling contact refers to the relative angular motion between two bodies in contact about an axis parallel to their common tangent plane [5]. Rolling, in general, results in an increase in contact area and a subsequent modification of the Hertzian stress field in both dry and lubricated conditions. The most critical influence on subsurface stress fields, however, is exerted by sliding. To illustrate the effect of sliding on the stress distribution, consider two bodies in contact with some sliding occurring between them. Frictional forces are the inevitable result of sliding and cause a shear stress to act along the interface [4].
Stress contours diagram by Johnson [5] show that the principal shear stress is due to the combined normal pressure and tangential stress for a coefficient of friction μ = 0.2. It can clearly be seen that as friction force increases, the maximum shear stress moves towards the interface. Thus there is a gradual increase in shear stress acting at the interface as the friction force increases. This phenomenon is very important in crack formation and the subsequent surface failure [4] and is the focus of this analysis. Change in the stress depth with the increase of traction is the common practice in wheel-rail contact mechanics to identify the rail life with the shake down theory. This study focuses on the suitability of using PEEQ instead of shear stress to predict the rail life.

2 Finite element model

2.1 Development of pressure loaded three-dimensional finite element model

The development of the pressure loaded rail model closely follows the work done by Ringsberg et al [6]. The present rail model, developed for analysis, is 80 mm long. The model is divided into two parts, i.e. a bottom part and inner top part. The parts are meshed separately as shown in Figure 1 and Figure 2 respectively. The inner part is of primary concern as the pressure extends 8mm from the centre of the rail head and is 16mm in width in total. It is defined to a depth of 16mm at the centre of the rail head.

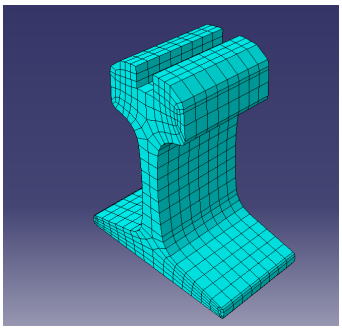

Figure 1. Mesh of the rail bottom part.

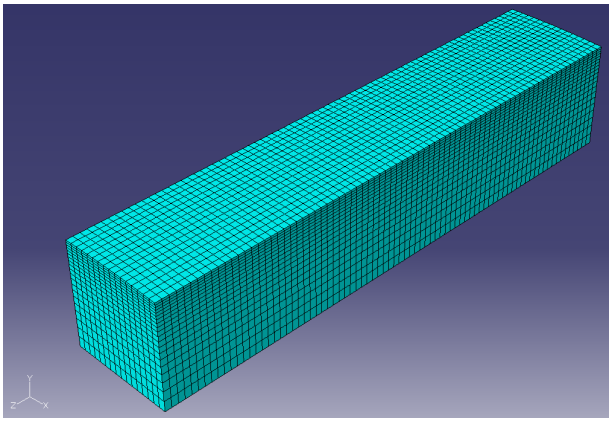

Figure 2. Meshed rail top.

The rail solid model as used for the analysis and generating results is shown in Figure 3. An elastic-plastic material model defines the materials in the rail top part, since this is the volume within which plastic deformation is likely to occur as a result of the wheel-rail rolling contact. The outer part represents the elastic surroundings of the rail, where only elastic deformation occurs, and is of less interest in the current investigation. The material of the outer part is therefore modelled using a linear-elastic material model. Therefore only a thin material layer in the vicinity of the wheel-rail contact region is assumed to experience plastic deformation. Additionally both parts are meshed by solid brick elements using a mapped option, i.e. a so-called structured mesh. The mesh density of the centre top part has a higher mesh density compared to the bottom part as clearly seen in Figure 3. The mesh density of the inner part gradually decreases downwards form the rail head surface. The mismatch between the element meshes of the adjoining surfaces between the inner and outer parts is controlled using the Abaqus “tie” constraint. This constraint causes adjoining surfaces to deform by equal measures.

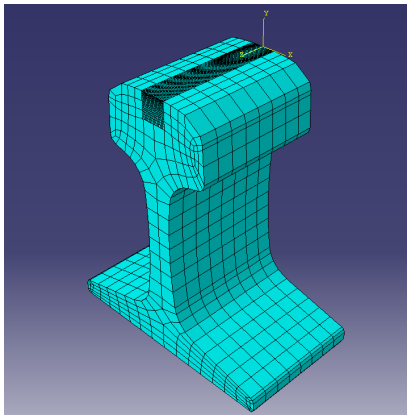

Figure 3. The full meshed rail model.

The distributions of contact load and traction load from the wheel-rail contact are applied to the centre of the rail top part by using Abaqus subroutines DLOAD and

UTRACLOAD. This analysis assumes single point contact even though it is unlikely in the practical scenario. During this analysis, a function using the coordinates as variables was used to describe the contact pressure as a Hertzian distribution. Therefore the 3-D Hertzian contact equations were used to define the contact ellipse semi-axes and the maximum contact pressure with the selected load condition [7] [8]. (A calculation summary is attached in Appendix 1.) All the degrees of freedom are restrained at the bottom of the rail model.

2.2 Material model

Bower [9] carried out uniaxial experiments for the normal grade rail steel and from the results several material models were developed to describe rail material behaviour. Kapoor et al [10] studied the material responses of an elastic-plastic material to cyclic loading and categorized them in to four categories depending on the stress-strain behaviour. The main focus in this publication is the study of stress and stress changes with increasing load. So the multiple cycles and the cyclic hardening parameters obtained by Kapoor are not considered in the current study.
Material models are described by constitutive equations governing the stress or the strain response for a material for a given stress or strain history. In the current study, the nonlinear isotropic /kinematic cyclic hardening model in Abaqus [1] was used to define classical metal plasticity. Even though cyclic hardening parameters were not studied, they were put on the material data section as all the considering material models in this study calculate the cyclic hardening parameters. The material model used [1] is the one developed by Chaboche and Lemaitre [11]. In the Chaboche model, there are five material parameters that need to be optimized. These material parameters were found from the literature. Four material models, which were developed mainly from the experimental results of Bower, can be found in the
Table **1**. Five parameters (c, γ, b, Q_∞, σ_0) were calibrated to uniaxial experimental data from cyclic tension-compression experiments on cylindrical specimens.
Four previously developed material models used different methods to calculate the parameters for their studies. 1997 Johansson and Thorberntsson [12] used Matlab [13] to optimised the five parameters in their case, using Bower's [9] experimental results as the basis for their study.
1999 Ringsberg et al [6] used the same model developed by Johansson and Thorberntsson [12] for his studies but the obtained material parameter values after Matlab optimization is differed to the one that previously obtained by Johansson and Thorberntsson So during this study it assumes that Ringsberg [6] follow the same method but he optimize the parameters to match his loading conditions and materials. For example the experimental data is from the uniaxial experimental data is not the best option for FE simulations that show multiaxial stress state response. In his simulations he takes the initial stress $\sigma 0$ from the experiments as 406 x 106 N/m^2.
The third material model parameters are the one produced by Ekh et al [14] in 2000 using the Armstrong-Frederick kinematic hardening model [15] and the isotropic hardening law. In their study Ekh et al consider three material models (A, B and J-S) and only the model A that consider for this study consider isotropic hardening

studied here. After the calibrations Ekh et al come up with parameters similar to the ones optimised by Johansson and Thorberntsson. The only difference is on the value "b" as can be seen in

Table **1**.
Fourth model is developed in 2001 by Schleinzer and Fischer [16] and they carried the optimization for the normal grade rail steel UIC 900A. This study has a significant improvement over the other three models explain above. It published the data up to three back stresses. Multiple back stresses used in nonlinear kinematic hardening models to significantly improve the analysis results in the plastic hardening process. Multiple back stresses means in other terms is the several kinematic hardening components. The results were validated with the uniaxial cyclic test that they performed.

	Johansson & Thorberntsson	Ringsberg et al	Ekh et al	Schleinzer & Fischer
σ_0 (MPa)	543	406	543	379
Q_∞(MPa)	22.8	152	22.8	189
γ	0.81	3.12	0.81	55,600,2000
b	0.47	3.97	10.7	500
c (MPa)	6490	13200	6490	24750,60000,200000
E(MPa)	209000	209000	209280	206000
v	0.29	0.29	0.29	0.28
ρ(kg/m^3)	7820	7820	7820	7820

Table 1. Material properties of the different models.

The density of the rail material was only given in the Ringsberg model. So the same density is used amongst all four models as the density of normal grade material is mostly similar.

3 Wheel-rail data and loading conditions

3.1 Rail track and wheel dimensions

The rail and wheel dimensions for the present model have been taken from Ringsberg [6]. The wheel radius at the running circle for the motor coach as 0.46m and the radius of the rail head at the axis of symmetry is 0.3m. The rail track was

considered to be straight and it was assumed that contact occurs at the centre of the rail head.

3.2 Loading conditions

In this study, a load distribution consistent with a theoretical Hertzian contact patch was applied to the rail-head. The semi-axes of the contact patch were calculated using the method described in the Appendix 1: Calculation of Hertzian contact parameters. The rail and wheel dimensions and the material properties as defined previously were used to complete the calculations.
The axle load of 14 tonnes, corresponding to a rail normal force of 70000 N, was used for the current investigation of all four models. The friction force was applied as a proportion of the normal force by multiplying the normal force by the friction coefficient. The two forces were applied as Abaqus subroutines DLOAD and UTRACLOAD. The details of the subroutines were discussed in the Abaqus subroutine manual [17].
The objective of this study was to document the change of stress and strain in the contact patch under changing friction coefficient, i.e. the effect of traction on the stress and strain behaviour in wheel-rail contact. All of the material parameters were kept constant in the above four models, with the friction coefficient on the rolling direction changing from 0.00 to 0.40 in 0.05 intervals.

4 Results from the finite element simulations

Graph 1 below shows the summary of the finite element analysis results along the rail cross section. The selected path was exactly at 40mm (midpoint) along the analysed small rail length.
Figure 4 shows the path considered for analysis. The data was taken by changing the friction coefficient from 0 to 0.40 by 0.05 intervals after one wheel pass.

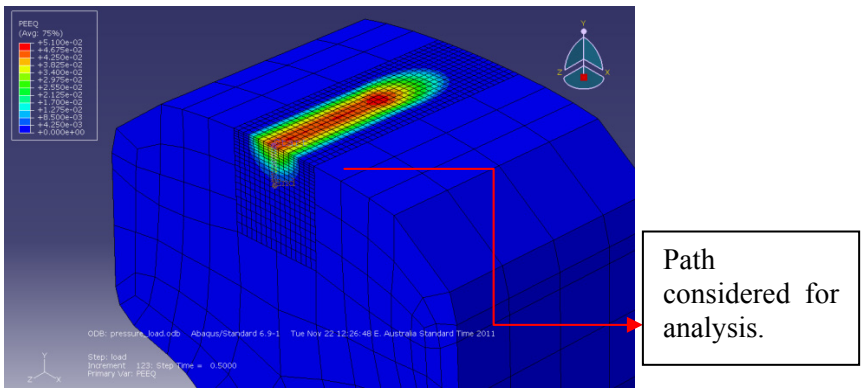

Figure 4. The path considered for the analysis.

Nine different analyses were carried out with different friction coefficient values for the material model data of Ringsberg [6] The effect of the increase in friction coefficient can be understood from Figure 5. . This compares the PEEQ distribution

at the midpoint along the rail length. As the friction coefficient increases the Maximum PEEQ generating point comes to the surface of the contact bodies.

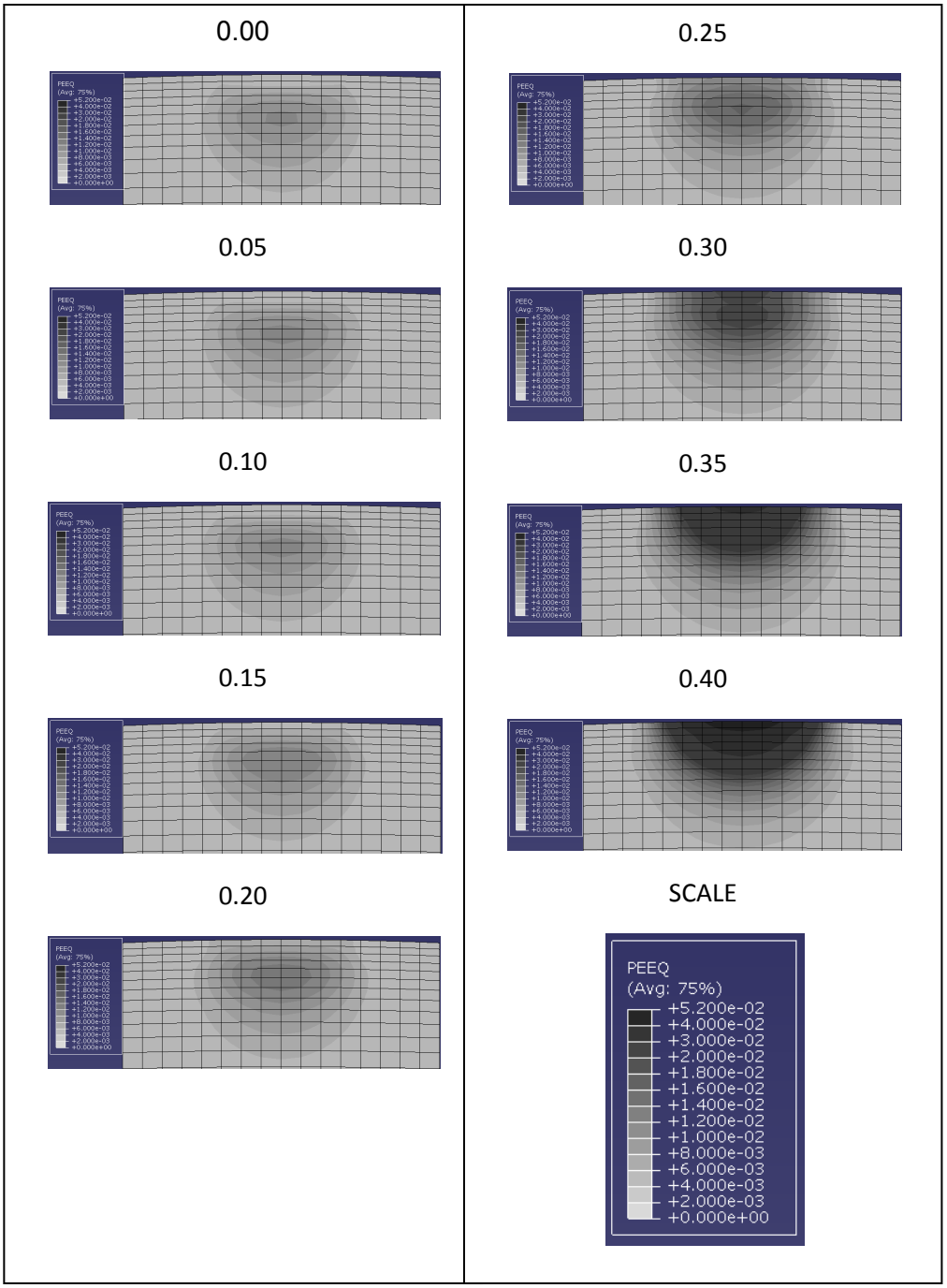

Figure 5. The effect of friction coefficient to the distribution of PEEQ along the rail head for Ringsberg et al [6] material model parameters.

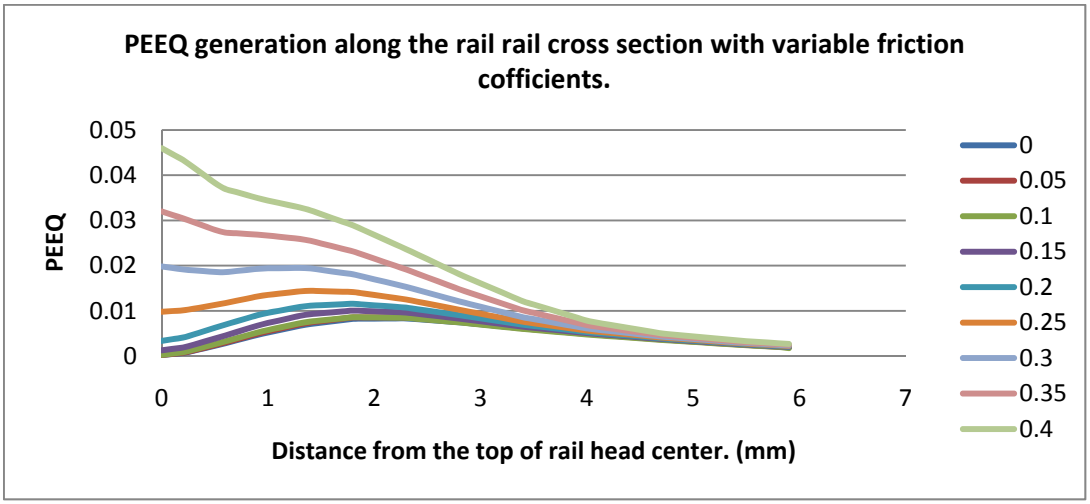

Graph 1. PEEQ generation along the rail cross section with different friction coefficients 0-0.40. According to Ringsberg et al [6] model parameters.

Graph 1 provides the summary of the nine different analyses carried out at different friction coefficients. For the friction coefficients 0 (which is no friction), 0.05, 0.10, 0.15, 0.20 and 0.25 the maximum PEEQ is below the rail top. But with the increase in the friction coefficient which is traction, the maximum PEEQ comes close to the rail top surface. The starting range is around 0.3.

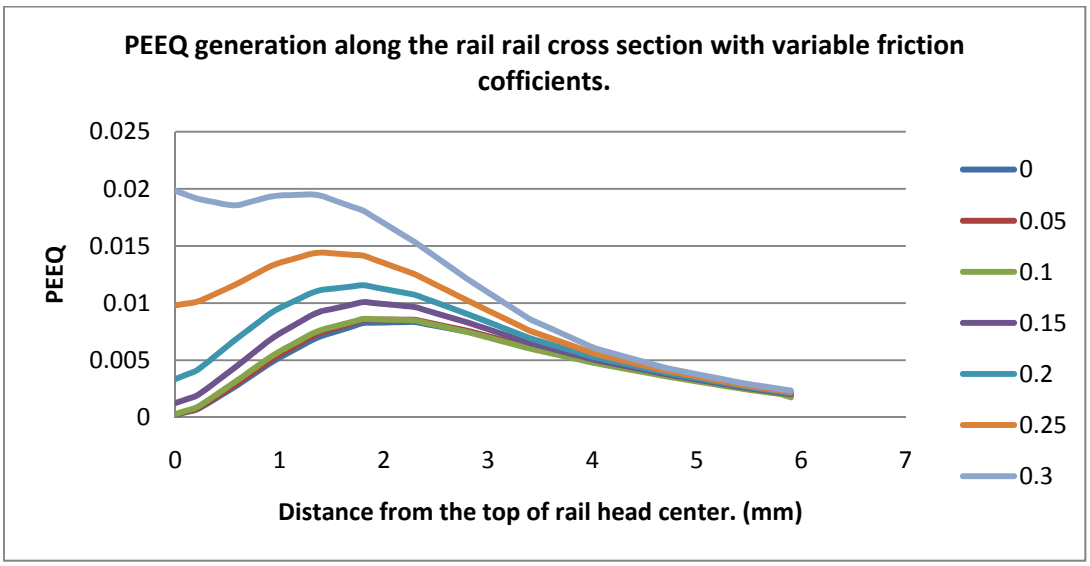

Graph 2. PEEQ generation along the rail cross section with different friction coefficients 0-0.30. According to Ringsberg et al [6] model parameters.

Graph 2 is considering only the first seven analysis of the Graph 1, where clear indication of the PEEQ changes can be found.

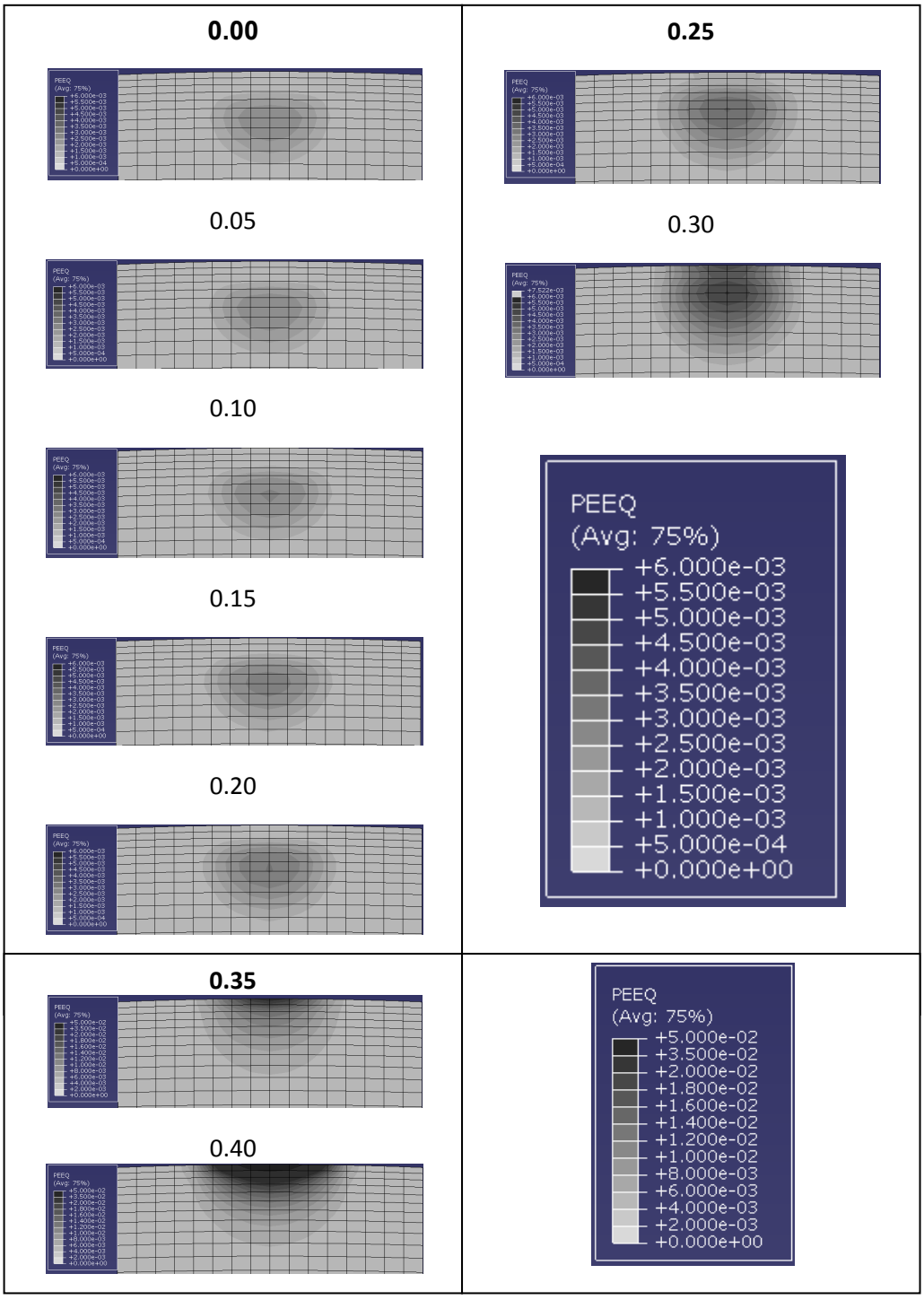

Figure 6. The effect of friction coefficient to the distribution of PEEQ along the rail head for Johansson and Thorberntsson [12] material model parameters.

Figure 6 shows the ABAQUS images of the rail head PEEQ generation with changes in friction coefficients 0-0.40 with 0.05 increments. The last two sets shown with different scale as it is helpful to identified differences in first seven images.

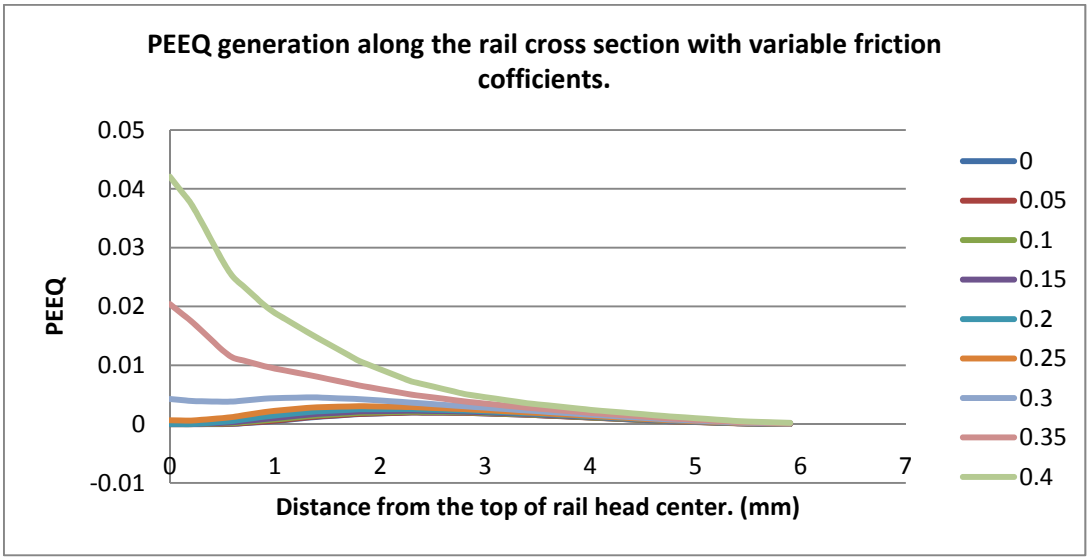

Graph 3. PEEQ generation along the rail cross section with different friction coefficients 0-0.40. According to Johansson et al [12] material model parameters.

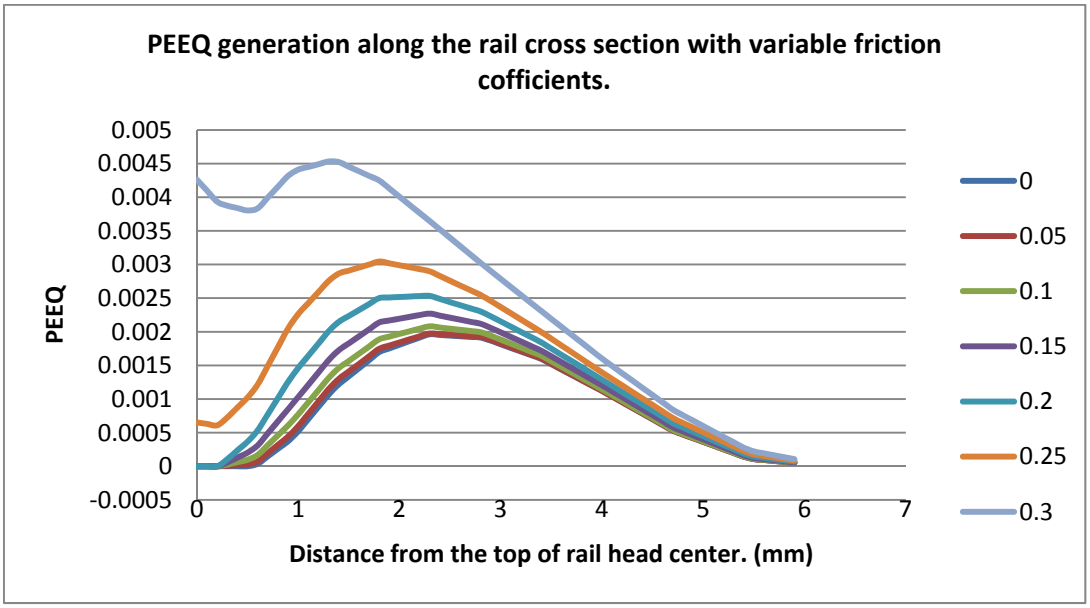

Graph 4. PEEQ generation along the rail cross section with different friction coefficients 0-0.30. According to Johansson et al [12] material model parameters.

Graph 4 is considering only the first seven analysis of the Graph 3, where clear indication of the PEEQ changes can be found.

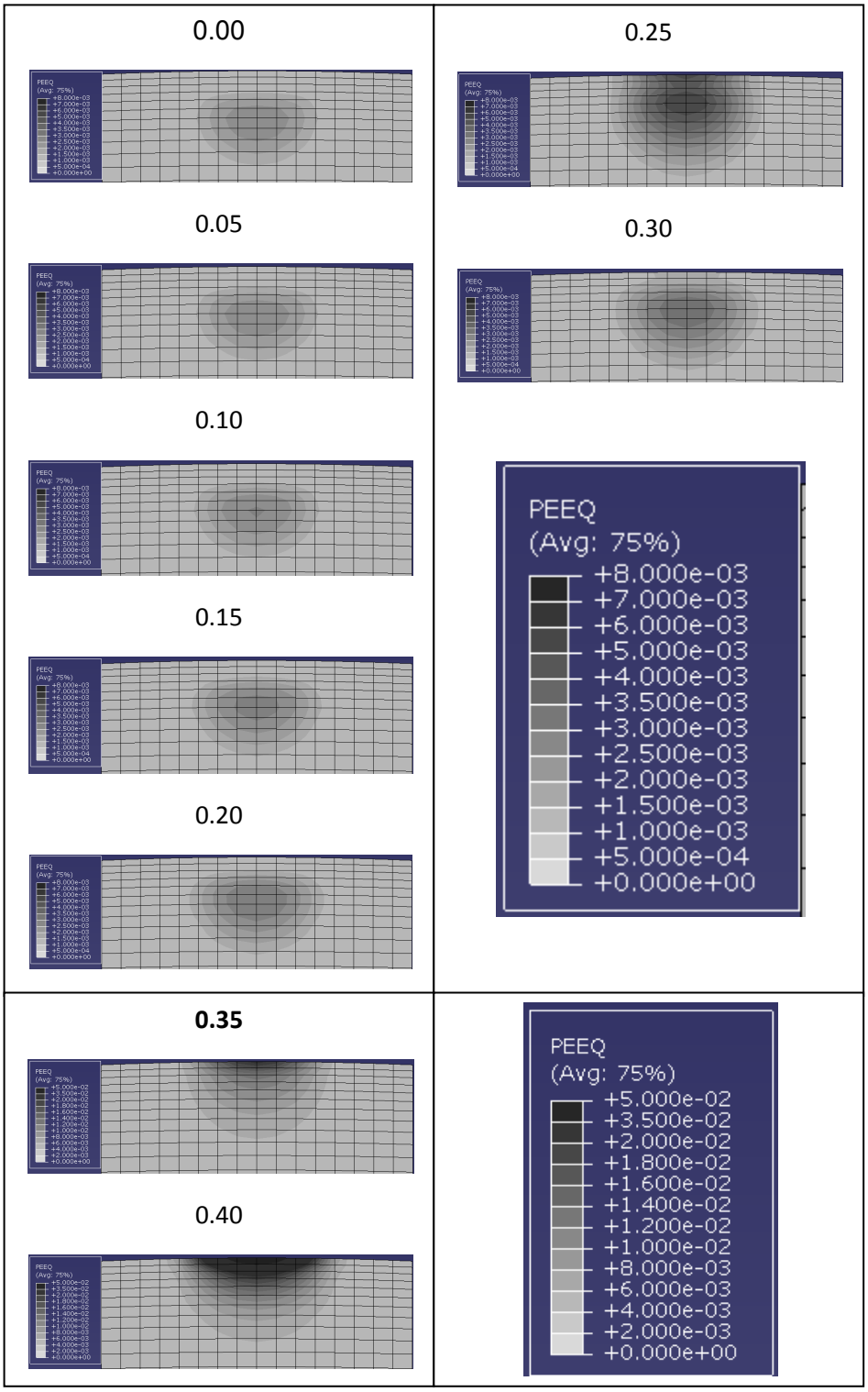

Figure 7. The effect of friction coefficient to the distribution of PEEQ along the rail head for Ekh [14] material parameters.

Figure 7 shows the ABAQUS images of the rail head PEEQ generation with changes in friction coefficients 0-0.40 with 0.05 increments. The last two sets

shown with different scale as it is helpful to identified differences in first seven images.

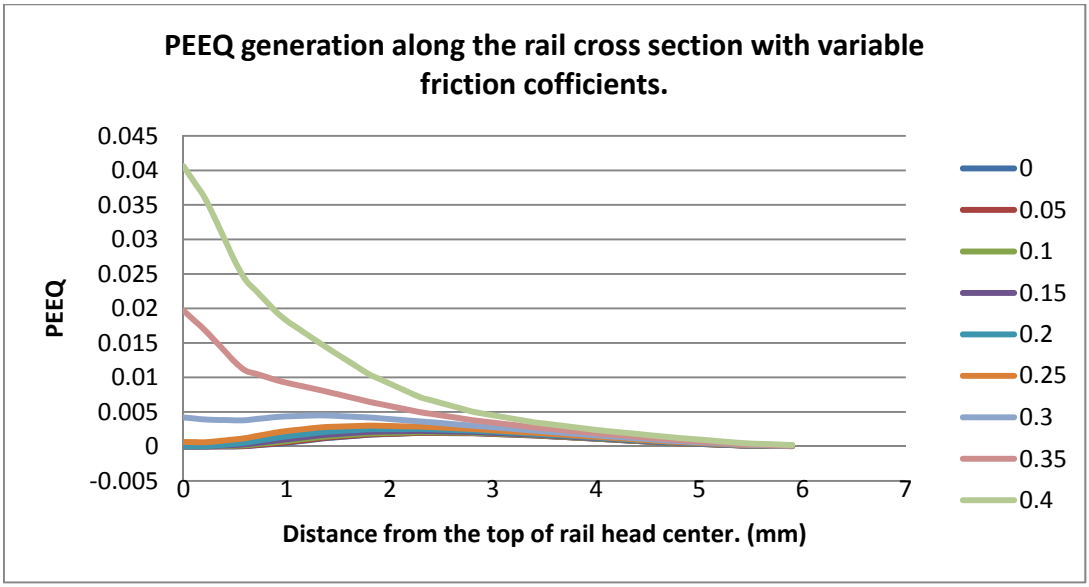

Graph 5. PEEQ generation along the rail cross section with different friction coefficients 0-0.40. According to Ekh [14] material parameters.

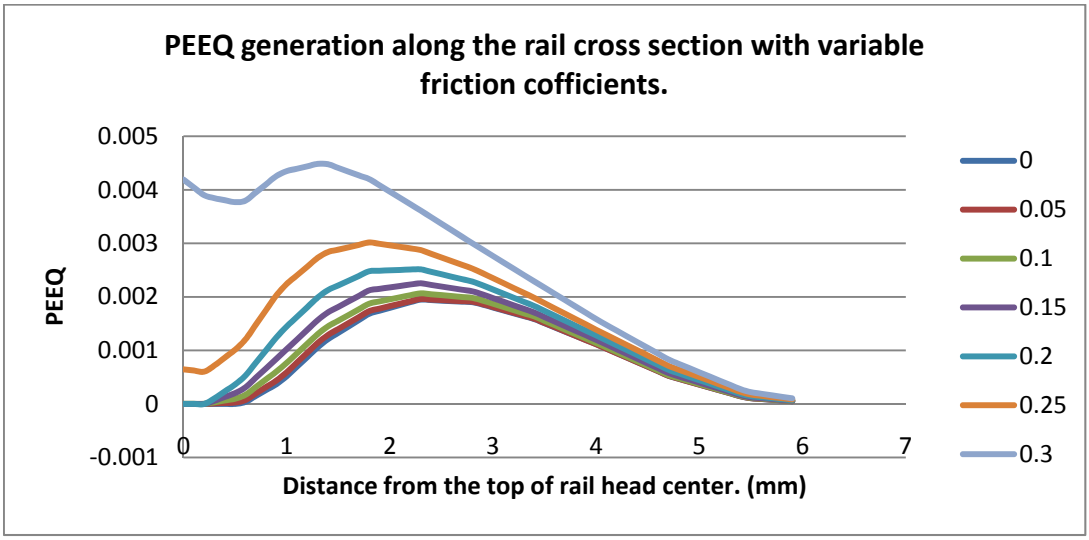

Graph 6. PEEQ generation along the rail cross section with different friction coefficients 0-0.30. According to Ekh [14] material parameters.

Graph 6 is considering only the first seven analysis of the Graph 5, where clear indication of the PEEQ changes can be found.

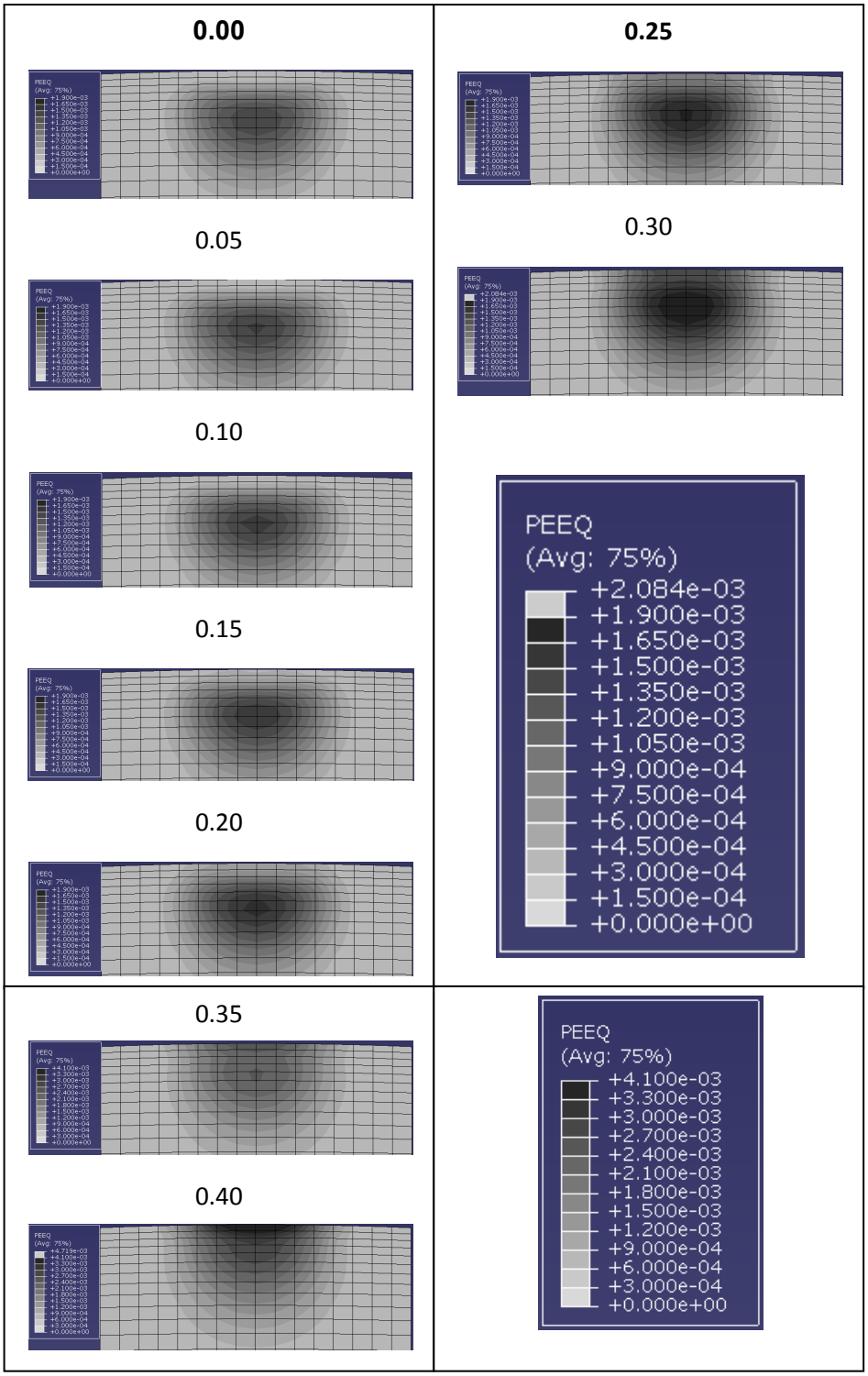

Figure 8. The effect of friction coefficient to the distribution of PEEQ along the rail head for Schleinzer & Fischer [16] material model parameters.

Figure 8 shows the ABAQUS images of the rail head PEEQ generation with changes in friction coefficients 0-0.40 with 0.05 increments. The last two sets shown with different scale as it help to identify the differences in first seven images.

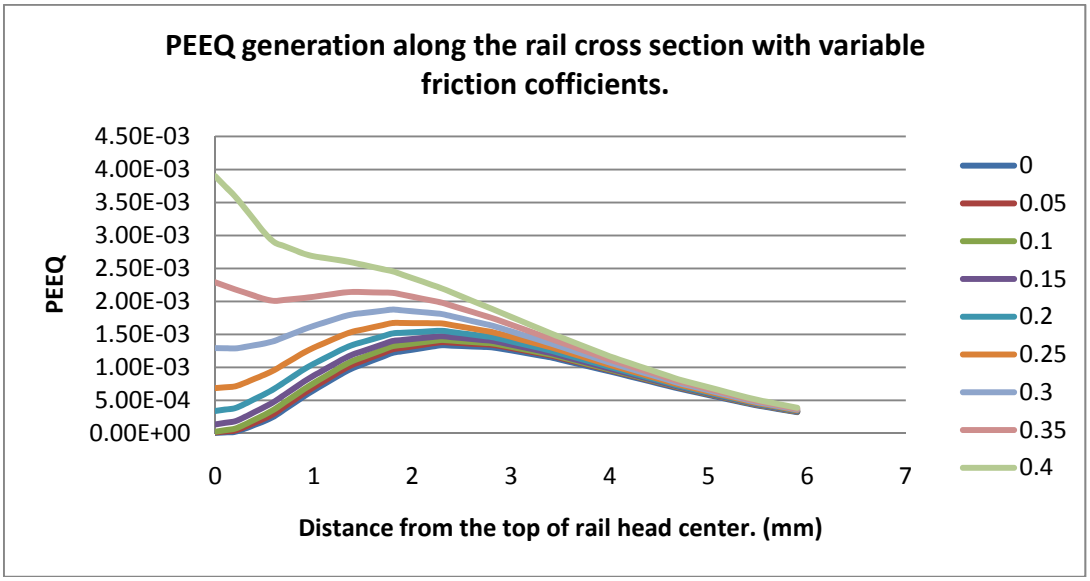

Graph 7. PEEQ generation along the rail cross section with different friction coefficients 0-0.40. According to Schleinzer & Fischer [15] material model parameters.

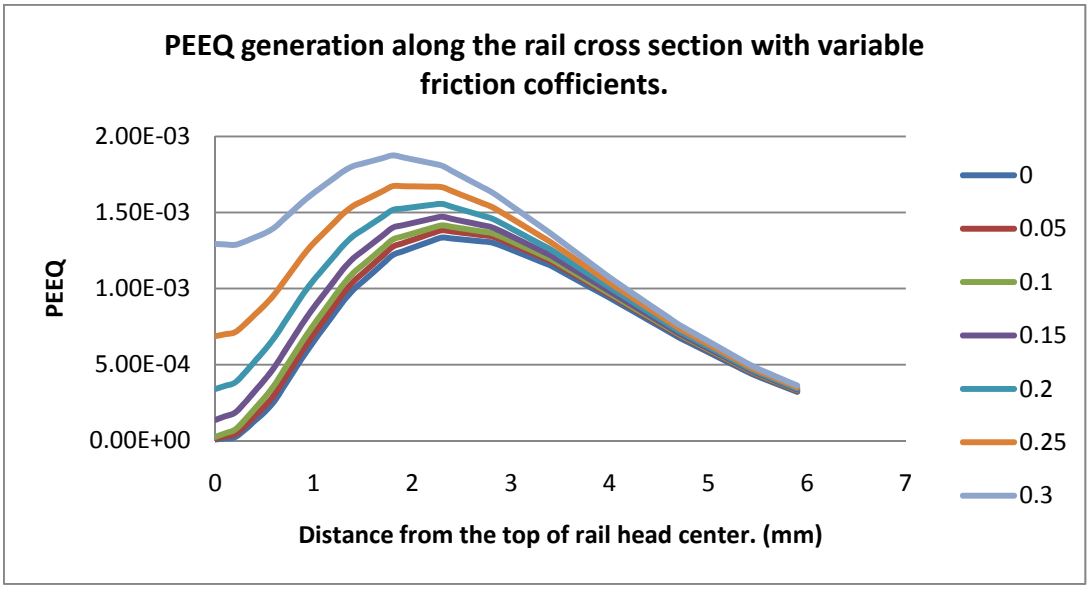

Graph 8. PEEQ generation along the rail cross section with different friction coefficients 0-0.30. According to Schleinzer & Fischer [16] material model parameters.

Graph 8 is considering only the first seven analysis of the
Graph 7, where clear indication of the PEEQ changes can be found.

5 Discussion

It is important to identify from the above summarised (Table 1) material parameters were used only two material models data. First material model developed by Johansson and Thorberntsson [12] is the base model used by Ringsberg et al [6] and Ekh et al [14] which actually Johansson and Thorberntsson are also authors of the publications. All three models used the results from Bower [9] experiments The second model developed by Schleinzer & Fischer [16] is for the rail steel UIC 900A is based on their own experiment results and methodology using Caboche's [11] model. So during the discussion main focus to discuss the two models considering Ringsberg et al [6] results and the Schleinzer & Fischer [16] results.

Kapoor [18] study the material failure with low cycle fatigue due to close strain and ratchetting failure due to open strain. Further in to his researches with Franklin [19] Kapoor investigate the wear and crack initiation using shear stress distribution on the rail head with different friction coefficients. The previous researches consider the shear stress distribution as the Finite Element Model data output to predict the life of rail material. The main objective in this research is to identify the in PEEQ with the traction changes. Previous studies of Johnson [5] found a mathematical method to calculate the depth of the contact surface where maximum stress occurs. In his calculations he numerically investigates the point where maximum shear stress occurs and it can be prove using the Finite Element modelling as well.

The problem with the consideration of shear stress is that with the higher contact loads the maximum stress comes close to the surface even without the traction load. The Graph 9 below is taken from the analysis with 0.00 friction coefficient (i.e. without traction) at 70kN load. The elements 1-9 taken along the rail cross section at the 40mm length (half of the total length). The history output Von Misses Stress taken for the whole period. At this loading condition the maximum stress almost reached at the third element which is 0.6mm from the rail top surface. It is already close to the rail top. At the same loading condition the maximum PEEQ is at the 6^{th} element which is 1.9mm below the surface which is shown in Graph 10. The next comparison is for the same elements with the 0.3 friction coefficient (where the maximum PEEQ reached to the rail top while increase from 0.0 friction coefficient). Here the maximum PEEQ at the rail top surface and decreased gradually till the 9^{th} element.

So the uses of PEEQ giving more range in terms of cross section depth to achieve its maximum value. And the other advantage of using PEEQ as FEM output is that it is not necessary to use history output data as the strain change is available at the end of the analysis. In Graph 10 and Graph 12 it is clear that after 0.4 seconds we can get the strain changes. With stress, we have to use history output data to track the stress values.

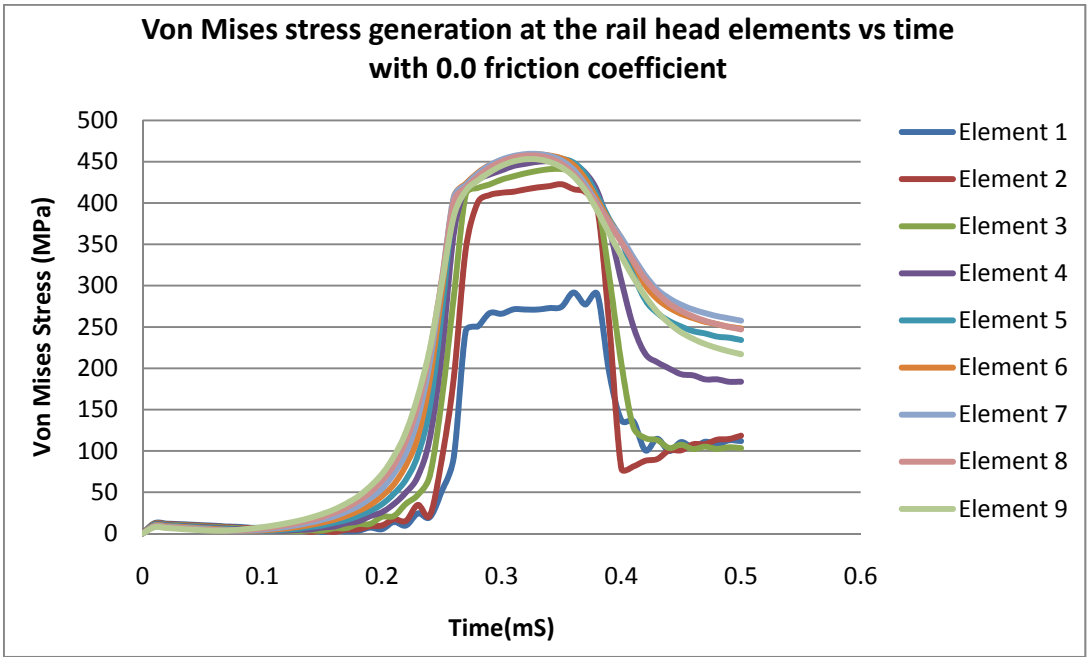

Graph 9. Von Misses Stress Vs Time of nine elements at the centre of the rail length, along the cross section with no traction.

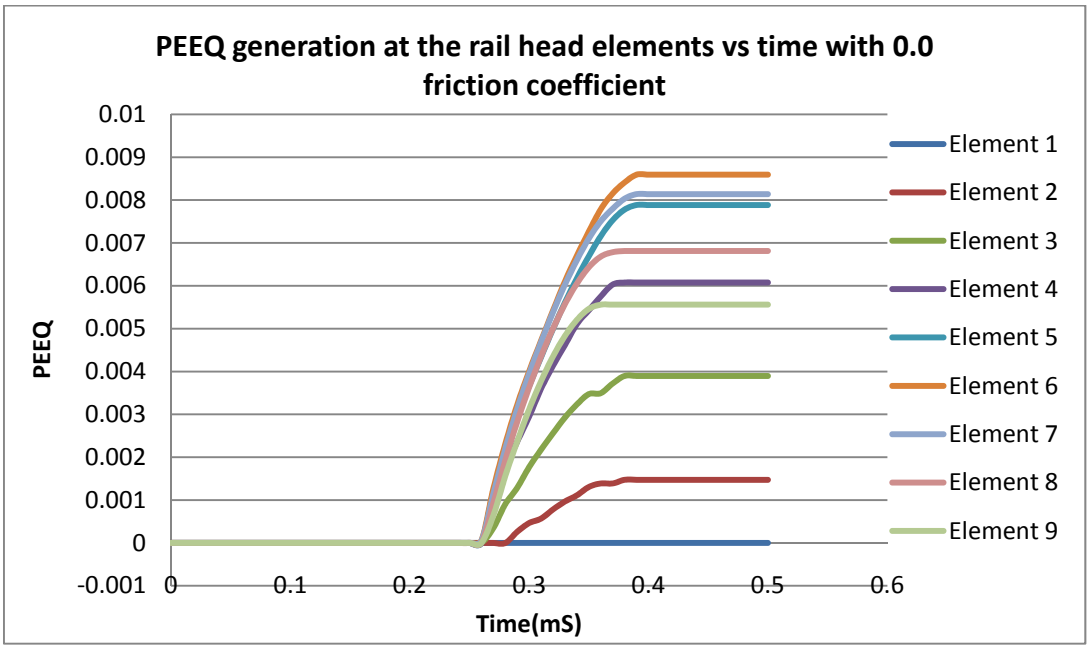

Graph 10. PEEQ Vs Time of nine elements at the centre of the rail length, along the cross section with no traction.

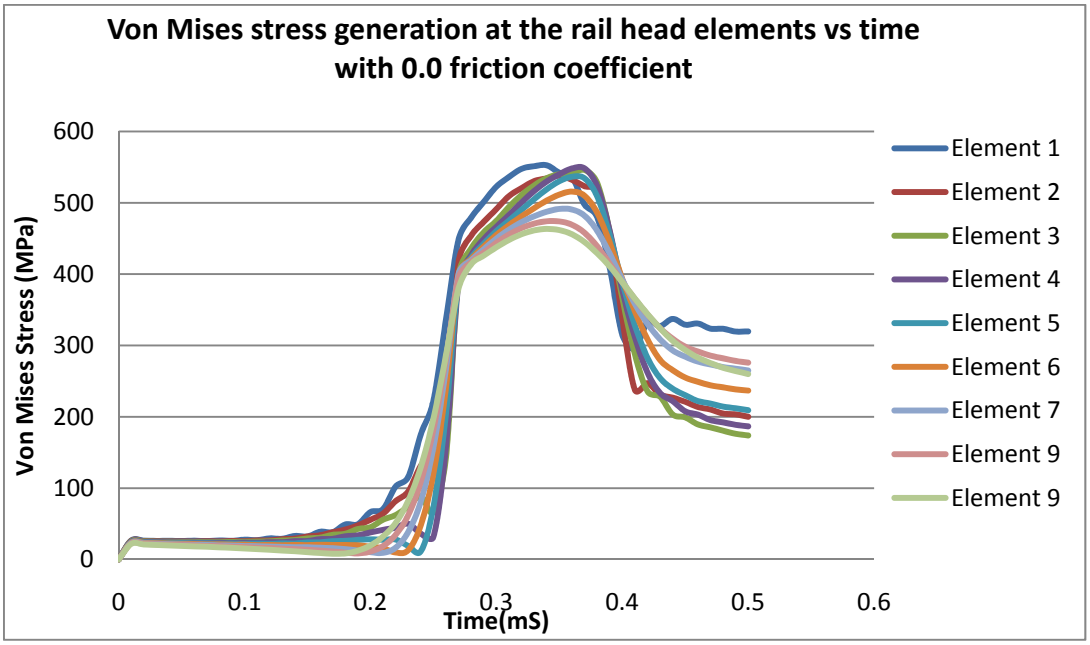

Graph 11. Von Misses Stress Vs Time of nine elements at the centre of the rail length, along the cross section with 0.3 friction coefficient.

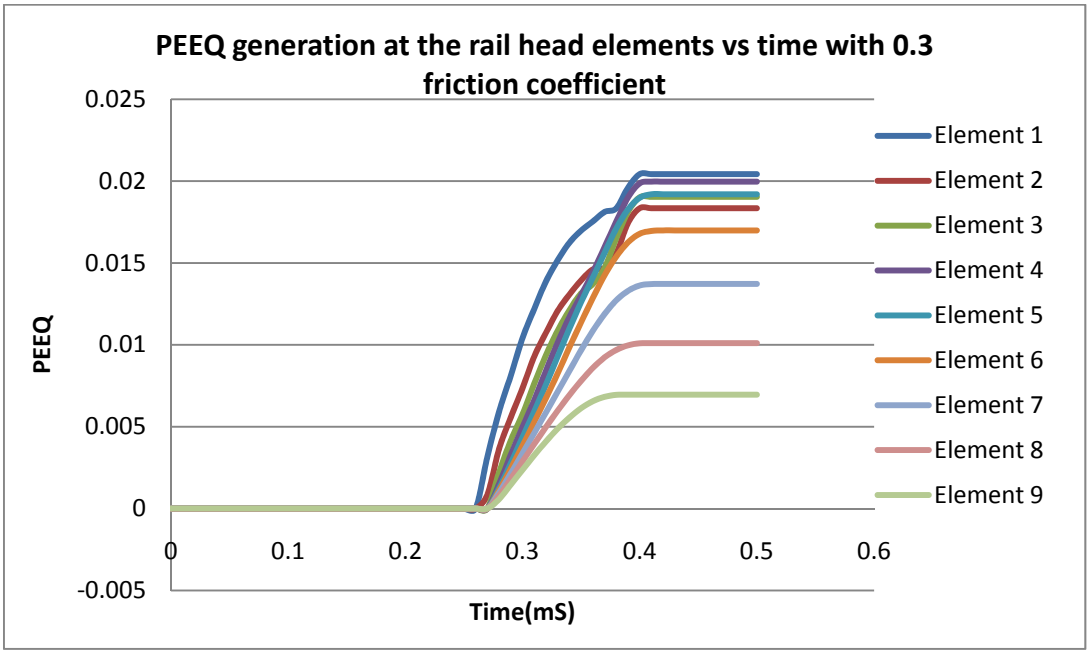

Graph 12. PEEQ Vs Time of nine elements at the centre of the rail length, along the cross section with 0.3 friction coefficient.

6 Conclusions

Based on the analysed models and results, it is concluded,

- At lower traction levels with higher vertical loads, the maximum PEEQ is generated at a higher depth below the surface than to the maximum misses' stress.
- At the 0.0 friction coefficient (zero traction) level maximum PEEQ is at 1.9mm below the surface and maximum misses' stress at 0.3mm below the surface. At the 0.3 friction coefficient maximum PEEQ reaching the surface in all analysed material models where it is gradually decreased along the rail cross section. So the PEEQ is a better parameter to study the rail wear.
- That this phenomenon can be use with previously developed ratchetting theory to predict the rail life.

Acknowledgement

The authors are grateful to the CRC for Rail Innovation (established and supported under the Australian Government's Cooperative Research Centres program) for the funding of this research. Project No.R3.110 Curve Lubrication.

References

[1] Abaqus, Abaqus/CAE 6.9-1: © Dassault Systèmes, 2009.
[2] H. Hertz, et al., Miscellaneous papers: Macmillan, 1896.
[3] A. A. Shabana, et al., "Contact and Creep-Force Models," in Railroad Vehicle Dynamics, ed: CRC Press, 2007, pp. 127-159.
[4] G. W. Stachowiak and A. W. Batchelor, "7 - Elastohydrodynamic Lubrication," in Engineering Tribology (Third Edition), ed Burlington: Butterworth-Heinemann, 2006, pp. 287-362.
[5] K. L. Johnson, Contact mechanics, 1st paperback (with corrections). ed. Cambridge: Cambridge University Press, 1987.
[6] J. Ringsberg, et al., "Rolling contact fatigue of rails—finite element modelling of residual stresses, strains and crack initiation," Proceedings of the Institution of Mechanical Engineers, Part F: Journal of Rail and Rapid Transit, vol. 214, pp. 7-19, 2000.
[7] Y. Chen and J. Kuang, "Contact stress variations near the insulated rail joints," Proceedings of the Institution of Mechanical Engineers, Part F: Journal of Rail and Rapid Transit, vol. 216, p. 265, 2002.
[8] A. A. Shabana, et al., Railroad vehicle dynamics : a computational approach. Boca Raton: CRC Press, 2008.
[9] A. Bower, "Cyclic hardening properties of hard-drawn copper and rail steel," Journal of the Mechanics and Physics of Solids, vol. 37, pp. 455-470, 1989.
[10] A. Kapoor and K. L. Johnson, "Plastic Ratchetting as a Mechanism of Metallic Wear," Proceedings: Mathematical and Physical Sciences, vol. 445, pp. 367-384, 1994.

[11] J. L. Chaboche and J. Lemaitre, Mechanics of Solid Materials. Cambridge: Cambridge University Press, 1990.
[12] A. Johansson and H. Thorberntsson, "Elastoplastic material model with nonlinear kinematic hardening for rolling and sliding contact fatigue," Degree of Master of Science, Department of Solid Mechanics, Chalmers University of Technology, Gothenburg, Sweden, 1997.
[13] MATLAB: (2007a, The MathWorks, City, State).
[14] M. Ekh, et al., "Models for Cyclic Ratchetting Plasticity-Integration and Calibration," Journal of Engineering Materials and Technology, vol. 122, pp. 49-55, 2000.
[15] P. J. Armstrong and C. O. Frederick, " A mathematical representation of the multiaxial bauschinger effect," CEGB Report RD/BJN731, 1966.
[16] G. Schleinzer and F. D. Fischer, "Residual stress formation during the roller straightening of railway rails," International Journal of Mechanical Sciences, vol. 43, pp. 2281-2295, 2001.
[17] Abaqus, Abaqus 6.9 Online Documentation: © Dassault Systèmes, 2009.
[18] A. Kapoor, "A re evaluation of the life to rupture of ductile materials by cyclic plastic strain.," Fatigue & Fracture of Engineering Materials & Structures, vol. 17, pp. 201-219, 1994.
[19] F. Franklin and A. Kapoor, "Modelling wear and crack initiation in rails," Proceedings of the Institution of Mechanical Engineers, Part F: Journal of Rail and Rapid Transit, vol. 221, pp. 23-33, 2007.
[20] A. A. Shabana, et al., "Numerical Procedure for the Simulation of Wheel/Rail Contact Dynamics," Journal of Dynamic Systems, Measurement, and Control, vol. 123, pp. 168-178, 2001.

Appendix 1: Calculation of Hertzian contact parameters.

According to the Hertzian contact theory, the contact area of a wheel and rail is elliptical in shape, with the major and minor semi-axis and b respectively. The contact pressure P distribution in this area can be expressed as [5]

$$P(z,x) = \frac{3F}{2\pi ab}\sqrt{1-\frac{z^2}{a^2}-\frac{x^2}{b^2}}$$

Where F is the applied normal load. According the developments of the FEM the z axis extends along the major axis and the x axis along the minor axis as shown in Figure 3. The magnitudes of axes a and b depend on the normal load, wheel and rail profiles and materials.

$$a = m\left(\frac{3\pi F(K_1+K_2)}{4K_3}\right)^{1/3}$$

$$b = n\left(\frac{3\pi F(K_1+K_2)}{4K_3}\right)^{1/3}$$

Where K_1 and K_2 are constants that depend on the material properties of the two bodies and are given as follows,

$$K_1 = \left(\frac{1 - V^{i^2}}{\pi E^i}\right) \quad and \;\; K_2 = \left(\frac{1 - V^{j^2}}{\pi E^j}\right)$$

Where E^i and E^j are the Young's modulus of elasticity of the two bodies and V^i and V^j are the Poisson ratios of the two bodies.
And K_3 is a constant that depends on the geometric properties (i.e. the principle radii of curvature of the surfaces of two bodies at the origin) of the two bodies and defined as follows,

$$K_3 = \frac{1}{2}\left(\frac{1}{R_1^i} + \frac{1}{R_2^i} + \frac{1}{R_1^j} + \frac{1}{R_2^j}\right)$$

The Coefficients m and n are given by Hertz in the Table 2 as a function of the angular parameter θ for the values 0^0 and 180^0 [2]where θ defined as,

$$\theta = cos^{-1}\left(\frac{K_4}{K_3}\right)$$

Where,

$$K_4 = \frac{1}{2}\sqrt{\left(\frac{1}{R_1^i} - \frac{1}{R_2^i}\right)^2 + \left(\frac{1}{R_1^j} - \frac{1}{R_2^j}\right)^2 + 2\left(\frac{1}{R_1^i} - \frac{1}{R_2^i}\right)\left(\frac{1}{R_1^j} - \frac{1}{R_2^j}\right)cos2\varphi}$$

φ is the angle of the orient difference in the principle axis of the two bodies. Also called yaw rotation. For the current study φ is taken as $0^{0.}$.

θ (deg)	*m*	*n*	*θ (deg)*	*m*	*n*	*θ (deg)*	*m*	*n*
0.5	61.4	0.1018	10	6.604	0.3112	60	1.486	0.717
1	36.89	0.1314	20	3.813	0.4125	65	1.378	0.759
1.5	27.48	0.1522	30	2.731	0.493	70	1.284	0.802
2	22.26	0.1691	35	2.397	0.530	75	1.202	0.846
3	16.5	0.1964	40	2.136	0.567	80	1.128	0.893
4	13.31	0.2188	45	1.926	0.604	85	1.061	0.944
6	9.79	0.2552	50	1.754	0.641	90	1.0	1.0
8	7.86	0.285	55	1.611	0.678			

Table 2. Hertz Coefficients m and n [3].

To use with the computer simulations and calculations, an alternative approach to the numerical interpolation is to develop closed-from expressions for the coefficients m and n as functions of θ. The following equations were proposed by Shabana et al [20].

$$m = A_m tan\left(\theta - \frac{\pi}{2}\right) + \left(\frac{\pi B_m}{\theta^{C_m}}\right) + D_m$$

$$n = \frac{1}{\left(A_n tan\left(\theta - \frac{\pi}{2}\right)\right) + 1} + B_n \theta^{C_n} + D_n sin\theta n$$

Where θ given in radians and the coefficients used for the Closed-Form Functions m and n is on the Table 3.

Coeff.	Value	Coeff.	Value
A_m	-1.086419052477	A_n	-0.773444080706
B_m	-0.106496432832	B_n	0.256695354565
C_m	1.350000000000	C_n	0.200000000000
D_m	1.057885958251	D_n	-0.280958376499

Table 3: Coefficients used for the Closed-Form Functions m and n [20].